Polarized spin and valley transport across ferromagnetic silicene junctions

V. Vargiamidis, and P. Vasilopoulos

Citation: Journal of Applied Physics **117**, 094305 (2015);
View online: https://doi.org/10.1063/1.4913934
View Table of Contents: http://aip.scitation.org/toc/jap/117/9
Published by the American Institute of Physics

Polarized spin and valley transport across ferromagnetic silicene junctions

V. Vargiamidis and P. Vasilopoulos
Department of Physics, Concordia University, 7141 Sherbrooke Ouest Montréal, Québec H4B 1R6, Canada

(Received 23 December 2014; accepted 20 February 2015; published online 5 March 2015)

We study ballistic transport of Dirac fermions through silicene barriers, of width d, with an exchange field M and metallic gates above them that provide tunable potentials of height U. Away from the Dirac point (DP), the spin- and valley-resolved conductances, as functions of U, exhibit resonances and close to it a pronounced dip that becomes a transport gap when an appropriate electric field E_z is applied. The charge conductance g_c of such a junction changes from oscillatory to a monotonically decreasing function of d beyond a critical E_z. This change of g_c can be used to realize electric-field-controlled switching. The field M splits each resonance of g_c in two spin-resolved peaks. The spin p_s and valley p_v polarizations of the current near the DP increase with E_z or M and become nearly perfect above certain of their values. We also show that p_s and p_v can be inverted either by reversing the polarity of U or the direction of M. For two barriers, there is no splitting in g_c when the fields M are in opposite directions. Most of these phenomena have no analogs in graphene. © *2015 AIP Publishing LLC*. [http://dx.doi.org/10.1063/1.4913934]

I. INTRODUCTION

Silicene, a monolayer of silicon atoms forming a two-dimensional (2D) honeycomb lattice, has been predicted to be stable[1] and several attempts have been made to synthesize it.[2,3] This new material has attracted considerable attention[4] due to the fact that it has Dirac cones which are similar to those of graphene.[5] However, contrary to graphene, silicene has a strong intrinsic spin-orbit interaction (SOI) which together with its buckled geometry leads to a gap approximately 1.55 meV wide[6,7] in the low-energy Dirac-like band structure. The buckled structure is a remarkable property of silicene that graphene does not possess and can facilitate the control[7,8] of its band gap by the application of an external perpendicular electric field E_z. Accordingly, silicene can overcome difficulties associated with potential applications of graphene in nanoelectronics (lack of a controllable gap) due to the available spin and valley degrees of freedom. This and its compatibility with silicon-based technology led to studies of important effects, such as the spin- and valley-Hall effects,[6,9–12] the quantum anomalous Hall effect,[8,13] and spin-valley coupling,[14] to name but a few. For a recent review see Ref. 15.

Spintronics aim to inject, manipulate, and/or use the spin degree of freedom in electronic devices. In contrast with graphene, the large value of SOI in silicene[16] not only can lead to spin-resolved transport but also to a cross correlation between the valley and spin degrees of freedom. Furthermore, silicon has a longer spin-diffusion time[17,18] and spin-coherence length[19] compared with graphene,[20] thus making silicene appear more suitable for spintronics applications.

In earlier works, several novel features have been studied, such as ferromagnetic (FM) correlations[21] and resonant transport through double barriers[22] in graphene, the anomalous magnetoresistance,[23] a valley-polarized quantum anomalous Hall effect in the presence of exchange,[24] and the conductance[25] across FM strips on the surface of a topological insulator, and valley and spin transport in FM silicene.[26,27] However, several important effects of the electric and exchange fields on transport of Dirac fermions in FM silicene have not been studied so far. Contrary to graphene, the field E_z greatly influences the transport properties of FM silicene because its band structures near the K and K' points shift in different ways.[13] This makes possible the control of spin and valley transport.

In this work, we systematically study charge, spin, and valley transport in silicene with a FM insulator on top of the sample and a metallic gate above it. The normal metal gate allows one to control the Fermi level locally and create a tunable barrier in silicene. First, we show that the charge conductance g_c through the junction can be either an oscillatory or a monotonically decaying function of the junction width d. One can interpolate between these two qualitatively different behaviours of g_c by varying E_z. Second, we show that g_c develops a transport gap with increasing E_z in an interval symmetric with respect to the Dirac point (DP). The physical origin of this gap is the fact that E_z acts like an extra "barrier": it does so for E_z large enough that transport via evanescent modes is completely suppressed. Notice that our subject differs from that of Ref. 28 in which different exchange fields apply to the two sublattices but no barrier is present and transport is not considered. Here we study transport properties in the presence of barriers and exchange fields which are the same for both sublattices and exist only in the barrier regions. In this way we can control the charge, spin, and valley conductances and the spin/valley polarizations by varying the barrier parameters and/or the exchange fields. Our study also differs from that of Ref. 24 which involves a uniform exchange field and no barriers.

Furthermore, we demonstrate that the presence of the FM insulator induces exchange splittings in silicene which are similar to those in graphene.[21] Due to the exchange splittings, the spin polarization near the DP increases with E_z or M and becomes nearly perfect above certain of their values. In addition, the spin and valley polarizations can be inverted either by changing the gate voltage U from negative to

positive or by reversing the direction of M. We also study the case of two magnetic gates a distance b apart. We find that the spin-up and spin-down conductances become identical when the exchange fields are in opposite directions and of equal magnitude resulting in the absence of exchange splittings. The results constitute a significant extension of our recent work.[29] In particular, the valley polarization in itself, the spin and valley polarization reversals just stated, an interpretation of the conductance behaviour vs the field E_z, with the help of the band structure near the two valleys, and some other results on single and double barriers are not part of this work.

The rest of the paper is organized as follows. In Sec. II, we present the calculation of the spin- and valley-resolved conductance through a FM junction in silicene and show that the charge conductance can be controlled with E_z. In Sec. III, we discuss the effects of the exchange field on the charge, spin, and valley transport, while in Sec. IV, we present our results for a double FM junction. Finally, we conclude with a summary in Sec. V.

II. TRANSPORT THROUGH A FERROMAGNETIC JUNCTION

We study ballistic electron transport across a FM strip in silicene with a metallic gate above it which extends over a region of width d (see Fig. 1(a)). The effective Hamiltonian of low-energy fermions is given by[16]

$$H_\xi = \hbar v_F(\tau_x k_x - \xi\tau_y k_y) + \Delta_{\xi s_z}\tau_z + U - s_z M; \tag{1}$$

Here, $\xi = \pm 1$ distinguishes between the two valleys, K and K', $\Delta_{\xi s_z} = \Delta_z - \xi s_z \lambda_{so}$, and $v_F \approx 5\times 10^5$ m/s is the Fermi velocity. The first term in Eq. (1) is the familiar Dirac-type Hamiltonian. The second term describes the intrinsic SOI in graphene, through λ_{so}, and controls the SOI gap through the perpendicular electric field term $\Delta_z = \ell E_z$ with $2\ell \approx 0.46$ Å the vertical separation of the two sublattices that is due to the buckled structure. The third term represents the barrier potential due to the gate voltage, and in the last term M is the proximity-induced exchange field due to a FM film. Furthermore, $s_z = \pm 1$ represents spin-up ($\uparrow$) and spin-down ($\downarrow$) states, and τ_i are the Pauli matrices of the sublattice pseudospin.

A. Tunnelling probability

We assume that the electric field is applied only in region II, $0 < x < d$, while $\Delta_z = 0$ in regions I and III. Due to the translational symmetry along the y axis, the

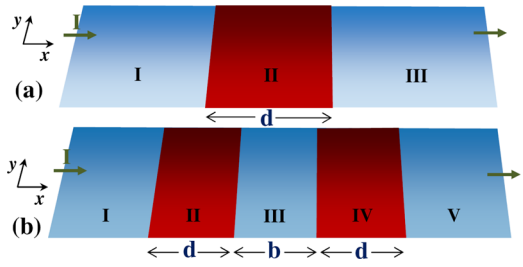

FIG. 1. Schematic representation of (a) a single and (b) a double FM junction in silicene.

eigenfunctions of Eq. (1) in regions I, II, and III can be written in terms of incident and reflected waves:

$$\Psi_I(\mathbf{r}) = \frac{e^{i(k_x x + k_y y)}}{\sqrt{2E_F E_N}}\begin{pmatrix} c_F e^{i\xi\theta} \\ E_N \end{pmatrix} + \frac{r_{\xi s_z} e^{i(-k_x x + k_y y)}}{\sqrt{2E_F E_N}}\begin{pmatrix} -c_F e^{-i\xi\theta} \\ E_N \end{pmatrix}, \tag{2}$$

$$\Psi_{II}(\mathbf{r}) = a_{\xi s_z} e^{i(k'_x x + k'_y y)}\begin{pmatrix} c'_F e^{i\xi\phi} \\ \epsilon_f \end{pmatrix} + b_{\xi s_z} e^{i(-k'_x x + k'_y y)}\begin{pmatrix} -c'_F e^{-i\xi\phi} \\ \epsilon_f \end{pmatrix}, \tag{3}$$

$$\Psi_{III}(\mathbf{r}) = \frac{t_{\xi s_z} e^{i(k_x x + k_y y)}}{\sqrt{2E_F E_N}}\begin{pmatrix} c_F e^{i\xi\theta} \\ E_N \end{pmatrix}. \tag{4}$$

Here, $c_F = \hbar v_F k_F$ and E_F is the Fermi energy measured from the DP. Furthermore, $E_N = E_F + \xi s_z \lambda_{so}$ and $\epsilon_f = E_F - U + s_z M - \Delta_{\xi s_z}$. The momentum of the incident particle makes an angle $\theta = \arctan(k_y/k_x)$ with the x axis. The corresponding angle inside the barrier is $\phi = \arctan(k'_y/k'_x)$. We have also defined

$$k_F = (k_x^2 + k_y^2)^{1/2} = (E_F^2 - \lambda_{so}^2)^{1/2}/\hbar v_F, \tag{5}$$

and

$$k'_F = [(E_F - U + s_z M)^2 - \Delta_{\xi s_z}^2]^{1/2}/\hbar v_F. \tag{6}$$

Due to the translational invariance along the y axis, the transverse momentum is conserved:

$$k_y = k'_y \Rightarrow k_F \sin\theta = k'_F \sin\phi. \tag{7}$$

The transmission amplitude associated with a particular spin in a particular valley, $t_{\xi s_z}$, is determined from the continuity of the wave function at $x = 0$ and $x = d$, i.e., from $\Psi_I(x = 0, y) = \Psi_{II}(x = 0, y)$ and $\Psi_{II}(x = d, y) = \Psi_{III}(x = d, y)$. The transmission at an angle of incidence θ is $T_{\xi s_z} = |t_{\xi s_z}|^2$ and has the form

$$T_{\xi s_z}(\theta) = \cos^2\theta\cos^2\phi/[\cos^2(k'_x d)\cos^2\theta\cos^2\phi + \sin^2(k'_x d)(\alpha + \alpha^{-1} - 2\sin\theta\sin\phi)^2/4], \tag{8}$$

where $\alpha = k_F\epsilon_f/k'_F E_N$ and

$$k'_x = [k'^2_F - k_F^2\sin^2\theta]^{1/2}. \tag{9}$$

Note that $T_{\xi s_z}(\theta) = 1$ for $k'_x d = n\pi$ with n integer, independent of the value of θ, as in the case of graphene. However, in contrast to graphene, for normal incidence ($\theta \to 0$ and $\phi \to 0$), we find that the transmission depends on the barrier height and deviates from unity

$$T_{\xi s_z}(0) = 1/[1 + \sin^2(k'_x d)(\alpha - \alpha^{-1})^2/4]. \quad (10)$$

We note that for a high barrier and any value of $k'_x d$, $T_{\xi s_z}(0) \to 1$ for either zero or nonzero Δ_z and M. Furthermore, by setting $\Delta_z = \lambda_{so} = M = 0$ we get $\alpha = 1$ and the well-known graphene result $T_{\xi s_z}(0) \to 1$.

The conductance pertinent to a particular spin in a particular valley through the barrier is obtained as

$$G_{\xi s_z} = G_0 \int_{-\pi/2}^{\pi/2} T_{\xi s_z}(\theta) \cos\theta d\theta = G_0 g_{\xi s_z}, \quad (11)$$

where $G_0 = e^2 k_F W/2\pi h$ with W the sample width along the y direction. The (dimensionless) spin-resolved conductance is defined as

$$g_{\uparrow(\downarrow)} = [g_{K\uparrow(\downarrow)} + g_{K'\uparrow(\downarrow)}]/2, \quad (12)$$

the valley-resolved one as

$$g_{K(K')} = [g_{K(K')\uparrow} + g_{K(K')\downarrow}]/2, \quad (13)$$

and the charge conductance as

$$g_c = g_\uparrow + g_\downarrow = g_K + g_{K'}. \quad (14)$$

Throughout this section, we take $E_F = 40$ meV, corresponding to a carrier density $n_e \simeq 5 \times 10^{-3}/\text{nm}^2$, $d = 110$ nm, and $\lambda_{so} = 3.9$ meV.

We show $g_\uparrow$ and $g_\downarrow$ in Fig. 2 as functions of U/E_F for zero electric and exchange fields, $\delta_z = \Delta_z/\lambda_{so} = 0$ and $m = M/E_F = 0$. As can be seen, in the absence of a FM film, $g_\uparrow$ and $g_\downarrow$ are identical because the band structures at both K and K' points are the same. This holds even for $\delta_z \neq 0$. The spin-resolved conductance exhibits resonance structure, for a high barrier or deep well, and oscillates between 2/3 and 1 away from the DP, see Eq. (17). This is due to the enhanced tunneling of Dirac fermions near normal incidence. The resonances are due to quasibound states which exist inside the potential barrier as in the case of graphene.[30] Note also that $g_{\uparrow(\downarrow)}$ exhibits a pronounced dip at the DP where the dominant contribution to transport is mainly due to evanescent modes, as explained in more detail in Sec. II B. At the DP, we have $U/E_F = 1$ and for

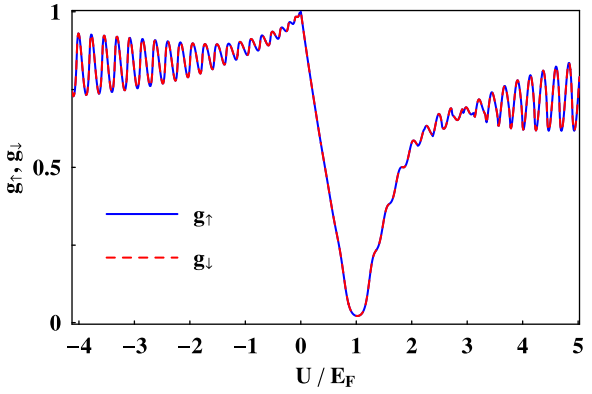

FIG. 2. Spin-resolved conductances $g_\uparrow$ and $g_\downarrow$ through a square barrier ($U \geq 0$) or well ($U \leq 0$) as functions of U/E_F for $\delta_z = \Delta_z/\lambda_{so} = 0$ and $m = M/E_F = 0$. Note that $g_\uparrow = g_\downarrow$ because the band structures at both K points are the same in the absence of the FM film.

$k_F d \gg 1$, we find that the spin- and valley-resolved conductance is given as (see Appendix A for details)

$$g_{\xi s_z} \approx (4\pi/q)^{1/2} e^{-2k_F d|\delta_{\xi s_z}|} \text{erf}(\sqrt{q}), \quad (15)$$

where $q = k_F d/|\delta_{\xi s_z}|$ with $\delta_{\xi s_z} = \Delta_{\xi s_z}/(E_F^2 - \lambda_{so}^2)^{1/2}$ and erf(x) the error function. As can be seen from Eq. (15), transport via the evanescent modes is progressively suppressed with increasing d or E_z and thus δ_z.

B. Tuning the conductance

From Eq. (8), we note that for a given θ, $T_{\xi s_z}(\theta)$ has an oscillatory (monotonically decaying) dependence on d provided k'_x is real (imaginary). From Eq. (9), we see that k'_x becomes imaginary whenever k'_F becomes imaginary (for k_F real) leading to spatially decaying modes in region II. Since k'_F depends on Δ_z, one can make k'_F imaginary by increasing the field E_z beyond the critical value $\Delta_z^c = \xi s_z \lambda_{so} \pm |E_F - U + s_z M|$. Thus we find that beyond a critical $\Delta_z = \Delta_z^c$, the transmission probability exhibits a monotonically decaying dependence on d. Consequently, for a thick enough barrier, one can tune the charge conductance g_c (at fixed E_F, U, and M) from a finite value to zero by tuning Δ_z through Δ_z^c. These qualitatively different behaviours of g_c for Δ_z below and above Δ_z^c are shown in Fig. 3(a) where we plot g_c as a function of the barrier width d for increasing values of δ_z. In general, for each pair (ξ, s_z), there is a separate value of Δ_z which yields a decaying behaviour of each $T_{\xi s_z}$. However, g_c exhibits a monotonically decaying dependence on d for the largest value, Δ_z^c, for which all four transmissions $T_{\xi s_z}$ exhibit separately such dependence. For this value, the Fermi level lies in the gap at both K and K' points, as discussed in the context of Fig. 4. We used $U/E_F = 2$ and $M = 2.5$ meV which yield the critical value $\delta_z^c = \Delta_z^c/\lambda_{so} = 11.9$. Note that $\delta_z = 1$ corresponds to $E_z = 0.17$ V/nm. Thus such a junction could be used as an electric switch. We point out that this effect has no analogue in graphene. This is due to the fact that in graphene $\Delta_{\xi s_z} = 0$ yielding $k'_F = |E_F - U|/\hbar v_F$ which cannot be made imaginary. In graphene, k'_x becomes purely imaginary only at the DP where $k'_F = 0$.

In Figs. 3(b) and 3(c), we show $g_\uparrow$ and $g_\downarrow$ as functions of d for $\delta_z = 7$ and $\delta_z = 10.8$, respectively. For $\delta_z = 7$, both $g_\uparrow$ and $g_\downarrow$ oscillate because the lowest values of δ_z required for them to exhibit a decaying behaviour are 10.62 and 11.9, respectively. However, for $\delta_z = 10.8$, $g_\uparrow$ exhibits a decaying behaviour, while $g_\downarrow$ oscillates. The reason is that for $\delta_z = 10.8$, E_F lies in the gap near the K point while it crosses the spin-down band at the K' point, see Fig. 4. This is also the origin of the large spin polarization discussed in Sec. III. In Fig. 3(d), we show the valley-resolved conductances, g_K and $g_{K'}$, for the same value of δ_z as in (c). It is seen that they exhibit a similar behaviour, i.e., $g_{K'}$ oscillates while g_K decays with d.

The tuning of the charge conductance can be understood from the band structures at the K and K' points as δ_z increases, see Fig. 4. The upper panels are for $\delta_z = 7$ and the lower ones for $\delta_z = 10.8$. Also, $M = 2.5$ meV. It can be seen that as the field E_z increases, the spin-split conduction bands

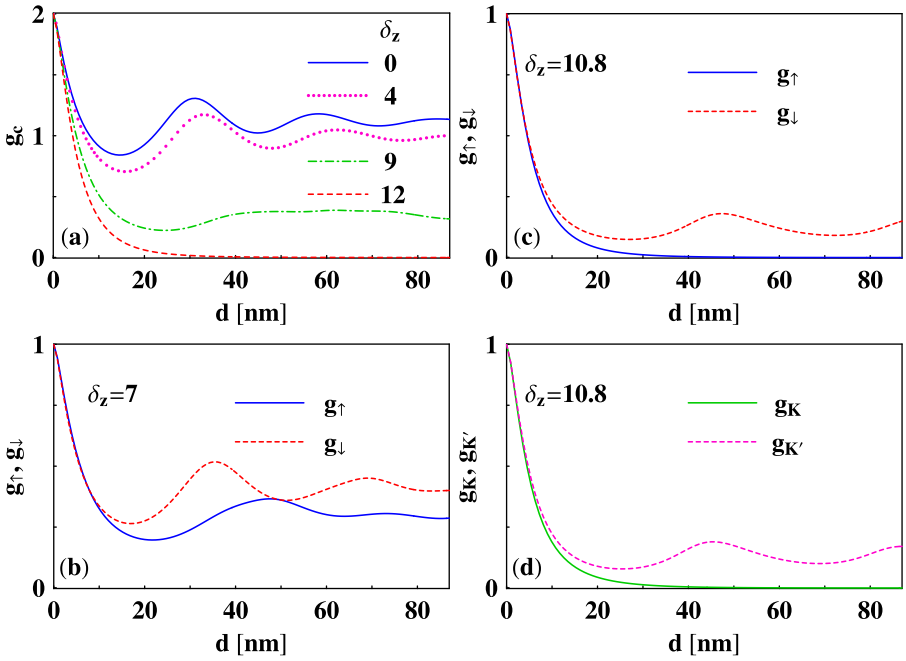

FIG. 3. (a) Charge conductance g_c as a function of the barrier width d for increasing values of δ_z. The critical value is such that $\delta_z^c = 11.9$ and corresponds to $E_z^c = 2.02\,\mathrm{V/nm}$. (b) Spin-resolved conductances $g_\uparrow$ and $g_\downarrow$ versus d for $\delta_z = 7$. (c) Same as in (b) but for $\delta_z = 10.8$. (d) Valley-resolved conductances g_K and $g_{K'}$ versus d for $\delta_z = 10.8$.

at both K and K' points shift upward. For $\delta_z = 10.8$, the bands at the K point shift so that E_F lies in the gap. However, at the K' point, E_F still crosses the spin-down band. Consequently, only evanescent modes contribute to $g_\uparrow$ leading to its monotonically decreasing behavior, while the current is entirely carried by spin-down electrons at the K' point leading to an oscillatory behaviour of $g_\downarrow$, as shown in Fig. 3(c). If δ_z is further increased above the critical value $\delta_z^c = 11.9$, E_F will be in the gap at both K and K' points and both $g_\uparrow$ and $g_\downarrow$ and consequently g_c will decay with d.

C. Transport gap

In Fig. 5(a), we show the charge conductance g_c as a function of U/E_F, in the absence of a FM insulator, for $\delta_z = 0$ and $\delta_z = 6$. It is seen that g_c develops a transport gap as the electric field increases from zero. It occurs because near the DP, $(|U/E_F| \approx 1)\, k'_F$ becomes imaginary for small δ_z, while away from it higher δ_z is needed. Away from the DP, the difference $|E_F - U|$ that appears in k'_F becomes larger and therefore higher δ_z^c is required to push the conduction bands upward and make k'_F imaginary. Thus, as δ_z increases (i.e., $|k'_x|$ increases), the evanescent modes for points away from the DP are gradually damped out; this creates the transport gap and the conductance vanishes. From Eq. (6) we see that for $M = 0$, the gap is described by

$$1 - \delta_F < U/E_F < 1 + \delta_F, \tag{16}$$

with $\delta_F = |\Delta_{\xi s_z}|/E_F$ and is symmetric with respect to the DP. The transport gap appears in all spin- and valley-resolved conductances labeled by a particular ξ and s_z. Equation (16) holds with $\xi s_z = +1$. However, if the electric field points in the opposite direction, Eq. (16) holds with $\xi s_z = -1$ for the

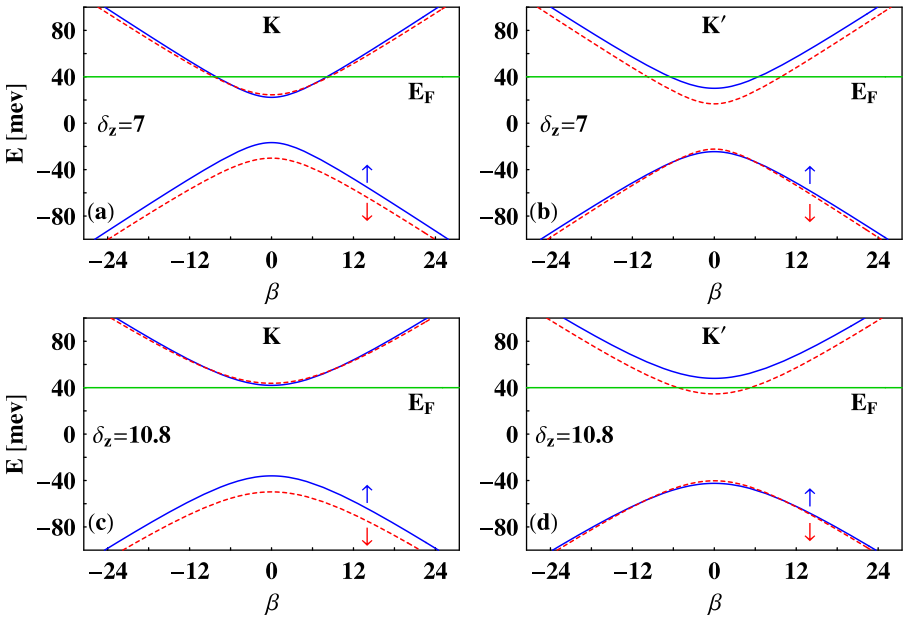

FIG. 4. Left panels. Energy dispersion E as a function of the dimensionless parameter $\beta = \hbar v_F k/\lambda_{so}$ at the K point, for two values of $\delta_z = \Delta_z/\lambda_{so}$. Right panels. As on the left but at the K' point. Note that for $\delta_z = 10.8$, the Fermi level (solid, green line) lies in the gap near the K point but crosses the spin down band at the K' point.

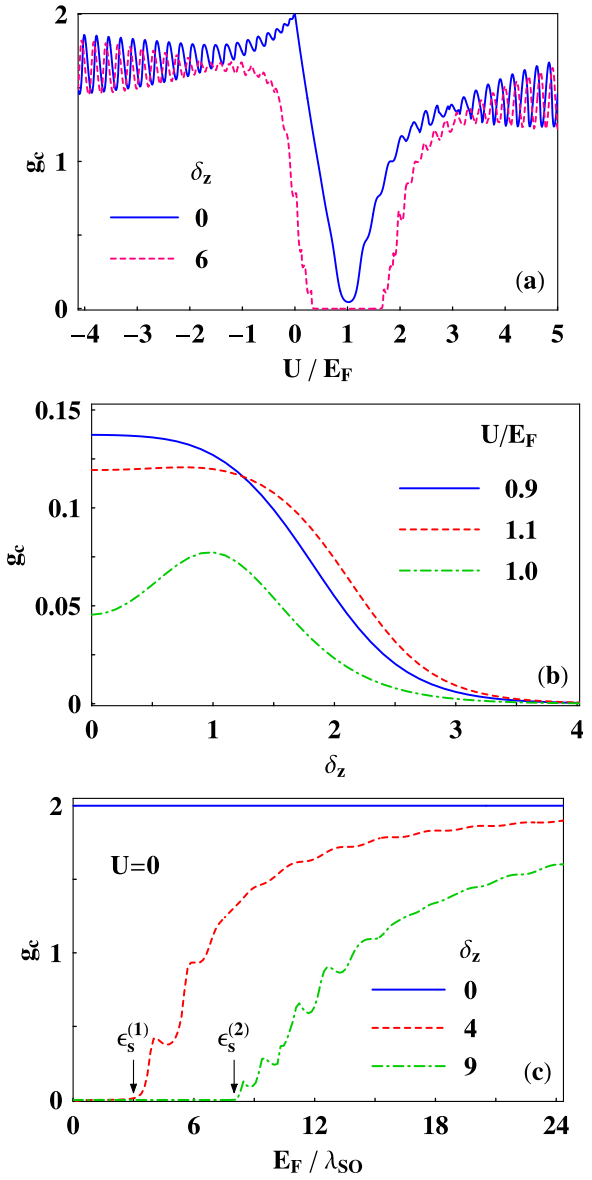

FIG. 5. (a) Charge conductance g_c as a function of U/E_F for $\delta_z = 0$ and $\delta_z = 6$. Note the appearance of a transport gap for $\delta_z = 6$. (b) g_c as a function of δ_z for three values of the gate voltage near the DP. (c) g_c as a function of $\epsilon_s = E_F/\lambda_{so}$ in the absence of a barrier ($U = 0$) for increasing values of δ_z. k_x' becomes imaginary below the critical values $\epsilon_s^{(1)}$ and $\epsilon_s^{(2)}$ and results in a vanishing conductance.

same reasons mentioned in Sec. II B. Note also that for $U/E_F = 0$, i.e., in the absence of a barrier, $g_c = 2$ for $\delta_z = 0$. However, for finite δ_z (dashed, red curve), there is no perfect transmission anymore, indicating that the electric field acts like an extra "barrier" in this region. We also note that a finite δ_z causes a shift in the conductance oscillations.

In Fig. 5(b), we show g_c as a function of δ_z for several values of U/E_F close to the DP. Note that near the DP, $U/E_F \approx 1$, g_c has a monotonically decaying dependence on δ_z for $\delta_z > 1$. This is because the contribution of evanescent modes gradually diminishes as δ_z increases, see Eq. (15). However, for $U/E_F = 1$, g_c first increases, reaches a maximum at $\delta_z = 1$, and then decreases. This maximum occurs because $|k_F'|$ at the DP decreases with δ_z and vanishes for $\delta_z \to 1$, resulting in smaller $|k_x'|$ and, consequently, larger contribution of the evanescent modes.

The effect discussed above can also be observed when no barrier is present ($U = 0$) by varying E_F for fixed, nonzero δ_z. In this case, g_c becomes finite only beyond a critical $E_F^c = \Delta_z - \lambda_{so}$ for which k_F' becomes real. For $E_F < E_F^c$, there are no propagating modes (k_F' becomes imaginary) and the conductance vanishes. This is shown in Fig. 5(c) where we plot g_c as a function of $\epsilon_s = E_F/\lambda_{so}$ for increasing values of δ_z and $U = 0$. As can be seen, below the critical values $\epsilon_s^{(1)} = E_F^{c1}/\lambda_{so} = 3$ and $\epsilon_s^{(2)} = E_F^{c2}/\lambda_{so} = 8$, the charge conductance vanishes. We also note that $g_c = 2$ when $\delta_z = 0$, as discussed in Fig. 5(a).

III. INFLUENCE OF THE EXCHANGE FIELD

Below we examine the effects of the exchange field M on the spin- and valley-resolved conductances. Throughout this section, we use $E_F = 40$ meV and $d = 110$ nm.

A. Spin-resolved conductance

In Fig. 6(a), we show the spin-resolved conductances $g_\uparrow$, $g_\downarrow$, and the charge conductance g_c as functions of U/E_F for $m = M/E_F = 0.058$ and $\delta_z = 0$. This value of m corresponds to exchange splitting $M = 2.32$ meV. As can be seen, the effect of M is to shift $g_\uparrow$ and $g_\downarrow$ relative to each other resulting in a broadening of the dip in g_c near the DP. Also, the shift of $g_\uparrow$ and $g_\downarrow$ drastically affects g_c for high barriers or deep wells, i.e., for $|U/E_F| \gg 1$. Specifically, the relative shift of $g_\uparrow$ and $g_\downarrow$ splits each resonance of g_c into two spin-resolved peaks with smaller amplitude, as will be discussed in the context of Fig. 7(a).

In Fig. 6(b), we show $g_\uparrow$, $g_\downarrow$, and g_c as functions of U/E_F for $m = 0.058$ but for finite $\delta_z = 6$. We note that both $g_\uparrow$ and $g_\downarrow$ develop transport gaps which are also shifted relative to each other, as expected. We also note that the effect of a finite δ_z is to shift the oscillations of g_c to the right relative to those for $\delta_z = 0$ while their amplitudes decrease. This is shown more clearly in Fig. 6(c) where we plot g_c versus U/E_F for $m = 0.058$ and the values of δ_z used in (a) and (b).

The relative shift of the oscillations in $g_\uparrow$ and $g_\downarrow$ is shown in Fig. 6(d) for the same parameter values as in (a). It is seen that $g_\uparrow$ and $g_\downarrow$ can differ substantially at a given value of U/E_F. We also note that all conductances are periodic functions of U/E_F, see explanation below.

Far from the DP, $|U/E_F| \gg 1$, we obtain an approximate analytical expression for the spin- and valley-resolved conductance (see Appendix B)

$$g_{\xi s_z} \simeq [|\gamma| - (1-\gamma^2)\mathrm{arctanh}(|\gamma|)]/|\gamma|\cos^2\omega, \qquad (17)$$

with $\omega = k_F d\eta\delta_\lambda$, $\gamma = \delta_\lambda \cos\omega/[1-\delta_\beta^2\cos^2\omega]^{1/2}$, $\delta_\lambda = [1-(\delta_{\xi s_z}^2/\eta^2)]^{1/2}$, and $\delta_\beta^2 = \delta_{\xi s_z}^2/\eta^2$. The parameter η is given in Eq. (A1). Equation (17) is in very good agreement with the exact numerical calculation of g_c (see dashed, red line in Fig. 7(a)). From expression (17), we see that g_c is periodic in η with period $\pi/k_F d\delta_\lambda$, which implies that it is a periodic function of U/E_F for fixed M with period $T_u = \pi\hbar v_F/E_F d\delta_\lambda$. It is also periodic in M/E_F with the same period. For the parameter values used in this section, we get $T_u = 0.235$.

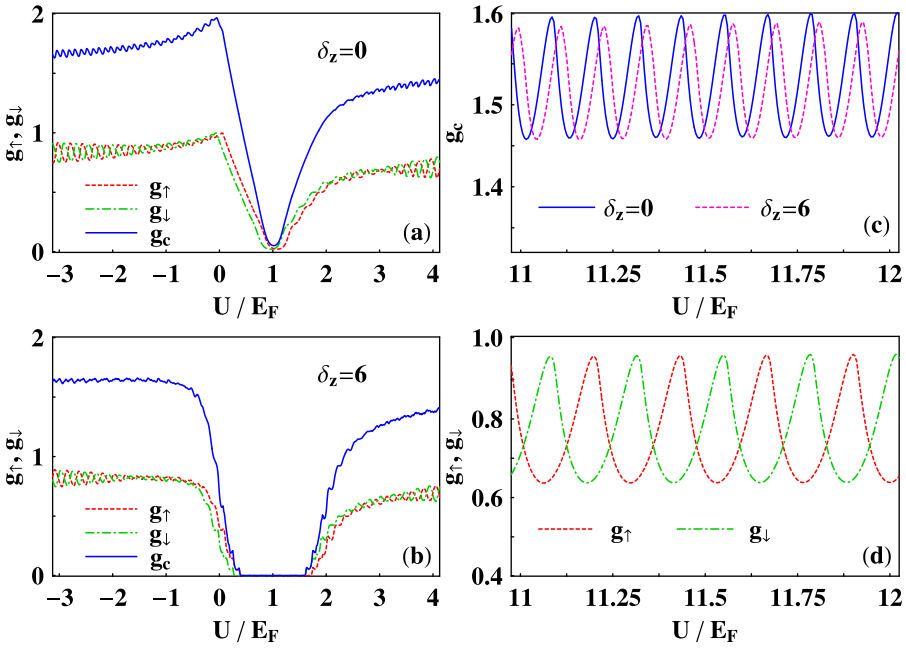

FIG. 6. (a) Spin-resolved conductances $g_\uparrow$ and $g_\downarrow$, and charge conductance $g_c = g_\uparrow + g_\downarrow$ as functions of U/E_F for $\delta_z = 0$ and $m = 0.058$. (b) The same as in (a) but for $\delta_z = 6$. (c) g_c as a function of U/E_F for $m = 0.058$, and the values of δ_z used in (a) and (b). (d) $g_\uparrow$ and $g_\downarrow$ as functions of U/E_F for the same parameters as in (a).

In Fig. 7(a), we show g_c versus U/E_F for $\delta_z = 0$ and several values of m. The curves are shifted upward in steps of 0.5. The dashed (red) line is calculated using the approximate expression (17) for $m = 0$. As can be seen, as m increases, each peak of g_c gradually splits into two spin-resolved peaks, a distance 2 m apart, of much smaller amplitude. This was also noted in the case of graphene.[21] As shown in Fig. 7(b), by further increasing M, such that $m = T_u/2$, the two spin-resolved peaks merge again to form one peak of large amplitude as in the case of $m = 0$. However, the peaks are now shifted by $T_u/2$ on the U/E_F axis relative to those for $m = 0$. For $m = 3T_u/4$, the peaks resolve again and become similar to those for $m = T_u/4$ shown in (a). For $m = T_u$, the spin-resolved peaks merge again but are also shifted by T_u on the U/E_F axis, i.e., they coincide with those for $m = 0$.

In Fig. 7(c), we show g_c as a function of m for several values of U/E_F which are close to the first peak in (a). Note the periodic variation of g_c as m increases with period T_u. We also note that for $m = T_u/2 \approx 0.117$, there is a minimum in g_c, whereas, as shown in (b), the two spin-resolved peaks merge to one of large amplitude. This minimum corresponds to the first minimum in g_c for $m = T_u/2$ in (b). Thus, a splitting of the conductance peaks occurs at the maxima of g_c vs m. This finding could be useful for the experimental determination of the exchange field for which proximity-induced splittings can be observed in ferromagnetic silicene.

B. Valley-resolved conductance

In Fig. 8(a), we show the valley-resolved conductances $g_K, g_{K'}$, and the charge conductance $g_c = g_K + g_{K'}$ as functions of U/E_F for $\delta_z = 6$ and $m = 0.04$. Contrary to the spin-resolved conductance, in the barrier (well) region, the field M splits the resonances of g_K and $g_{K'}$ into spin-resolved peaks of smaller amplitude. The splitting of the peaks of $g_{K'}$ in the barrier region is shown more clearly in Fig. 8(d), where we plot g_K and $g_{K'}$ versus U/E_F for the same parameter values as in (a). This is due to the fact that the valley symmetry is broken when $m \neq 0$, which implies that the bands at K and K' points shift in a different way as δ_z increases resulting in spin-resolved transport in one valley but not in the other.

In Fig. 8(b), we show $g_K, g_{K'}$, and g_c as functions of U/E_F for $\delta_z = 6$ and $m = T_u/4 = 0.058$. In this case, the shift of g_K and $g_{K'}$ relative to each other is such that it causes splitting of the peaks of g_c, which is similar to that in Fig. 6. This is shown more clearly in Fig. 8(c) where we plot g_c as a function of U/E_F for $m = 0.04$ and $T_u/4$ corresponding to (a) and (b).

C. Spin polarization

As usual, the spin polarization p_s is defined as

$$p_s = (g_\uparrow - g_\downarrow)/(g_\uparrow + g_\downarrow). \tag{18}$$

For $0 < p_s \leq 1$, the transmitted current is spin-up polarized, while for $-1 \leq p_s < 0$, its polarization is reversed.

In Fig. 9(a), we show the spin polarization p_s as a function of U/E_F for $m = 0.22$ and increasing values of δ_z. It is seen that p_s becomes more pronounced with increasing δ_z. This is mainly due to the fact that the spin-split conduction bands in the ferromagnetic region shift in a different way at the K and K' points with increasing δ_z, i.e., they shift upward faster at one valley than at the other one. Thus, for large δ_z, only a single spin band contributes to the current giving rise to large spin polarization. In addition, p_s becomes more pronounced because the evanescent modes are gradually suppressed as δ_z increases. For sufficiently large δ_z, the charge current becomes fully spin-polarized with spin-up electrons below the DP and spin-down electrons above it. The change of sign in p_s is directly related to the relative shift of the conductances $g_\uparrow$ and $g_\downarrow$. Thus, the spin current can be controlled by the electric field and p_s can be inverted by changing the gate voltage U from negative to positive.

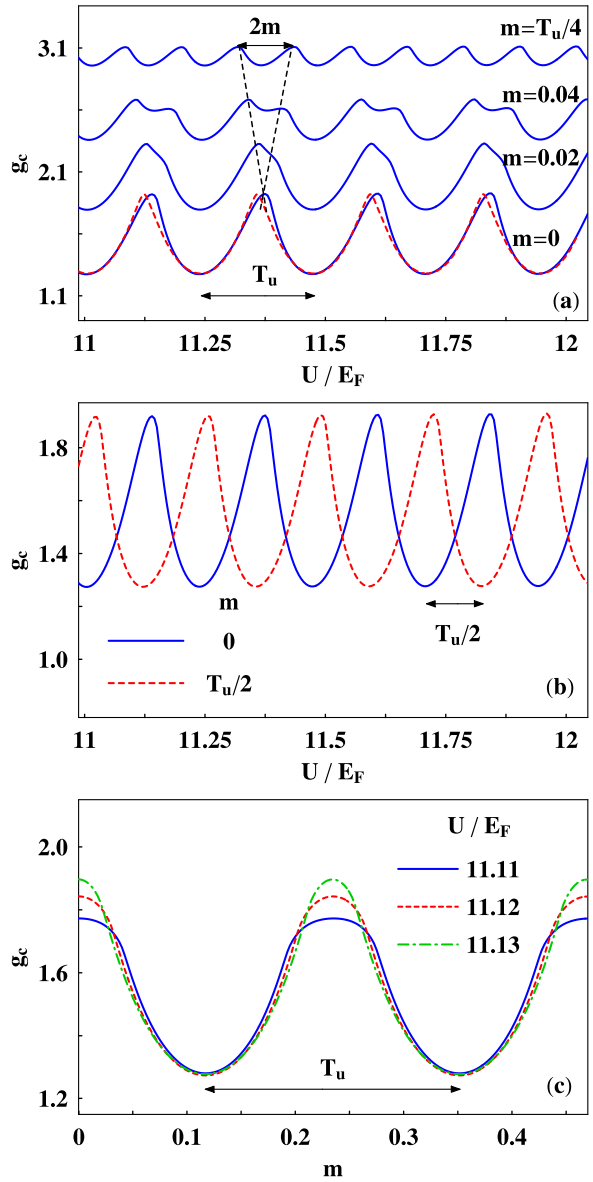

FIG. 7. (a) Charge conductance g_c versus U/E_F for $\delta_z = 0$ and several values of the exchange field m. The curves are shifted upward in steps of 0.5. The dashed (red) curve is computed using the approximate expression (17). (b) g_c versus U/E_F for $m = 0$ and $T_u/2$. (c) g_c versus m for three values of U/E_F close to the first peak in (a).

The spin polarization can also be controlled by varying the exchange field. This is shown in Fig. 9(b) where we plot p_s versus of U/E_F for $\delta_z = 5$ and increasing values of m. As in (a), fully spin-polarized current can be achieved for sufficiently large m, which is a consequence of the broken valley symmetry. In passing, we note that p_s becomes more pronounced with increasing width d.[26]

The spin polarization can also be tuned by changing the direction of the exchange field from positive to negative. This is shown in Fig. 10(a) where we plot p_s as a function of U/E_F for $\delta_z = 8$ and $m = \pm 0.22$. As can be seen, p_s is inverted by simply reversing the direction of the exchange field. For $m = 0.22$, the transmitted current is spin-up (spin-down) polarized below (above) the DP, while for $m = -0.22$, it becomes spin-down (spin-up) polarized. In Fig. 10(b), we show the valley polarization $p_v = (g_K - g_{K'})/(g_K + g_{K'})$ as a function of U/E_F for the same parameter values as in (a). It is seen that the sign of p_v can also be switched by reversing the direction of m. However, the regions of near-perfect valley polarization are shorter than those of p_s. In Fig. 10(c), we show p_s as a function of m for $U/E_F = \pm 1.7$ and $\delta_z = 8$. It is seen that as m changes sign, the spin polarization also changes sign. Above (below) the DP ($U/E_F = \pm 1.7$), p_s becomes negative (positive) as m becomes positive. As mentioned above, this is directly related to the relative shift of the conductances $g_\uparrow$ and $g_\downarrow$. This is shown in Figs. 10(d) and 10(e), where we plot $g_\uparrow$ and $g_\downarrow$, as functions of U/E_F, for $m = 0.06$ and -0.06, respectively. For $m = -0.06$, the shift of $g_\uparrow$ and $g_\downarrow$ relative to each other is opposite to that for $m = 0.06$. As a result, the sign of p_s changes when m is reversed. Similar considerations hold for p_v. These findings could be used to realize a silicene-based, high-efficiency spin- and valley-filter.

IV. DOUBLE FERROMAGNETIC JUNCTION

In this section, we study a double ferromagnetic junction shown schematically in Fig. 1(b). The magnetic gates, both of width d and a distance b apart, extend over regions II and IV, We assume that E_z is applied only in these regions and vanishes everywhere else.

The eigenfunctions are of the same form as those for a single ferromagnetic junction (see Sec. II A). In regions I, III, and V, k_F is given by Eq. (5) and $k_F^{(i)}$ in regions II and IV by Eq. (6) with $k_F' \to k_F^{(i)}$. Also, similar to Eq. (7), we now have $k_y = k_y^{(i)} \Rightarrow k_F \sin\theta = k_F^{(i)} \sin\phi_i$, $i = \text{II}, \text{IV}$, where $\theta = \arctan(k_y/k_x)$ is the angle that the incident particle makes with the x axis, and $\phi_i = \arctan(k_y^{(i)}/k_x^{(i)})$ the angle inside the first or second barrier. Applying the continuity of the wave function at the interfaces leads to a system of eight equations with eight unknowns which are solved numerically to obtain the transmission. We also defined the longitudinal momenta as in Eq. (9), that is, $k_x^{(i)} = [(k_F^{(i)})^2 - k_F^2 \sin^2\theta]^{1/2}$, $i = \text{II}, \text{IV}$. In the numerical calculation, we used $d = 100$ nm, $b = 50$ nm, and $E_F = 40$ meV. We also set $\delta_z = \delta_z^{(1)} = \delta_z^{(2)}$ the common value of the electric field in the two regions.

In Fig. 11, we show the charge conductance g_c as a function of the barrier width d for increasing values of δ_z. We used $U_1/E_F = 2$, $U_2 = U_1$, and the same exchange fields $m_i = M_i/E_F = 0.063$, $i = 1, 2$. We find that g_c decays exponentially with d beyond a critical value of δ_z, as in the case of a single barrier. In fact, the expression for the critical δ_z^c is the same as that for a single barrier. We note that it is sufficient to increase either $\delta_z^{(1)}$ or $\delta_z^{(2)}$ above δ_z^c in order to observe the exponentially decaying behaviour of g_c. For the parameters used here, the critical value is $\delta_z^c = 11.9$, the same as for a single barrier. We also note that a near-zero transmission is achieved faster because the two barriers together increase the effective width. Below $\delta_z^c = 11.9$, g_c remains oscillatory; however, the oscillation patterns are more complex.

In Fig. 12(a), we show $g_\uparrow$ as a function of V/E_F for two values of δ_z. We take $U_1 = U_2 = V$, i.e., the barriers have equal heights, and vanishing exchange fields, $m_1 = m_2 = 0$. In this case, $g_\downarrow = g_\uparrow$. We note that for $\delta_z = 0$, $g_\uparrow$ is almost

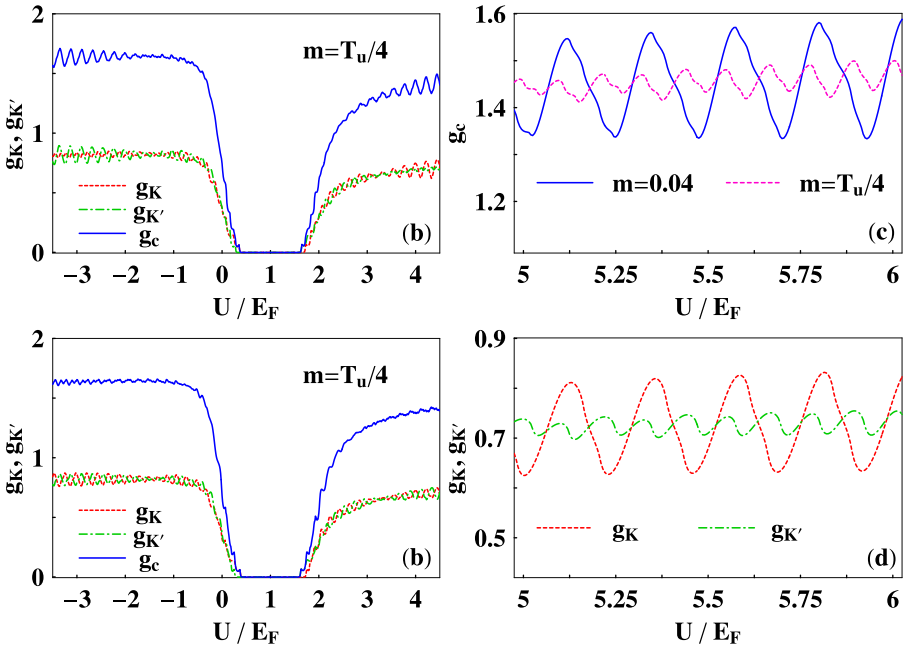

FIG. 8. (a) Valley-resolved conductances g_K and $g_{K'}$, and charge conductance g_c as functions of U/E_F for $\delta_z = 6$ and $m = 0.04$. (b) The same as in (a) but for $m = T_u/4$. (c) g_c vs U/E_F for $\delta_z = 6$ and the values of m used in (a) and (b). (d) Valley-resolved conductances g_K, $g_{K'}$, as functions of U/E_F for the same parameters as in (a).

zero at $V/E_F \approx 1$. This occurs because the two barriers together increase the effective width which causes a drastic suppression of transport through the evanescent modes. Also, increasing δ_z from zero leads to a transport gap similar to that for a single barrier. It has the same form as that for a single barrier and be found from an equation similar to Eq. (16) with the change $k'_F \to k_F^{(i)}$. We also note that the oscillatory pattern is the same as that for a single barrier but, for $\delta_z = 0$, it becomes slightly irregular in the barrier region.

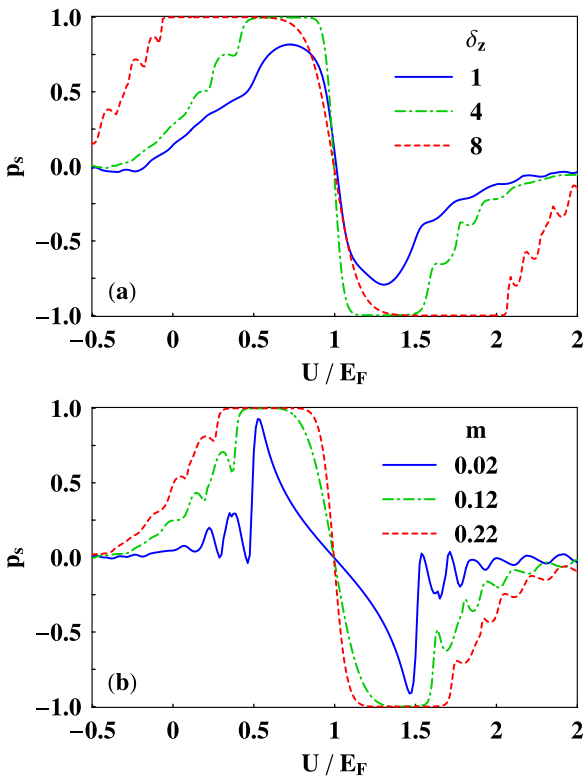

FIG. 9. (a) Spin polarization p_s as a function of U/E_F for $m = 0.22$ and increasing values of δ_z. (b) The same as in (a) but for fixed $\delta_z = 5$ and several values of m.

In Fig. 12(b), we show the charge conductance g_c as a function of $\epsilon_s = E_F/\lambda_{so}$ for $V = 0$, vanishing exchange fields $m_1 = m_2 = 0$, and increasing values of δ_z. We note that $g_c = 2$ for $\delta_z = 0$, as expected. We also note that g_c vanishes below a critical value of the Fermi energy, i.e., for $\epsilon_s < E_F^c/\lambda_{so}$ where $E_F^c = \Delta_z - \lambda_{so}$, for which $k_F^{(i)}$ becomes imaginary, as in the case of a single barrier.

For barriers (wells) of unequal height (depth), the conductance has a richer structure. In Fig. 12(c), we show $g_\uparrow$ as a function of V/E_F for $U_1 = V$ with $U_2 = 1.2V$ (solid, blue curve) and $U_2 = 0.8V$ (dashed, red curve). The electric and exchange fields are taken to be zero. First, it is seen that the dips are broadened and shift away from the DP. Second, the oscillation pattern in the barrier region becomes more complex and irregular. We also observe a beating pattern with progressively larger oscillations with increasing depth of the wells. We attribute the beating to the interference of Dirac fermions with slightly different energy due to the asymmetry of the two wells. This pattern is similar to that found for asymmetric electrostatic wells in graphene.[31]

In Fig. 12(d), we show $g_\uparrow$, $g_\downarrow$, and g_c as functions of V/E_F for $U_2 = 1.2U_1$. The electric and exchange fields are such that $\delta_z = 6$ and $m_1 = m_2 = 0.05$. It is seen that both $g_\uparrow$ and $g_\downarrow$ exhibit beating patterns in the well region. Also, the relative shift of $g_\uparrow$ and $g_\downarrow$ leads to irregular oscillations of g_c, especially in the barrier region, which cannot be used to determine the exchange splittings.

We demonstrate now the effect of the exchange fields on the spin-resolved and charge conductances. In Fig. 13(a), we show $g_\uparrow$, $g_\downarrow$, and g_c as functions of V/E_F for $\delta_z = \delta_z^{(1)} = \delta_z^{(2)} = 6$, $m_1 = m_2 = 0.05$, and for barriers of equal height $U_1 = U_2 = V$. As can be seen, the exchange fields shift $g_\uparrow$ and $g_\downarrow$ relative to each other resulting in splitting of the peaks in the charge conductance, as in the case of a single barrier. However, the amplitudes of the oscillations in $g_\uparrow$ and $g_\downarrow$ become much larger than those for a single barrier

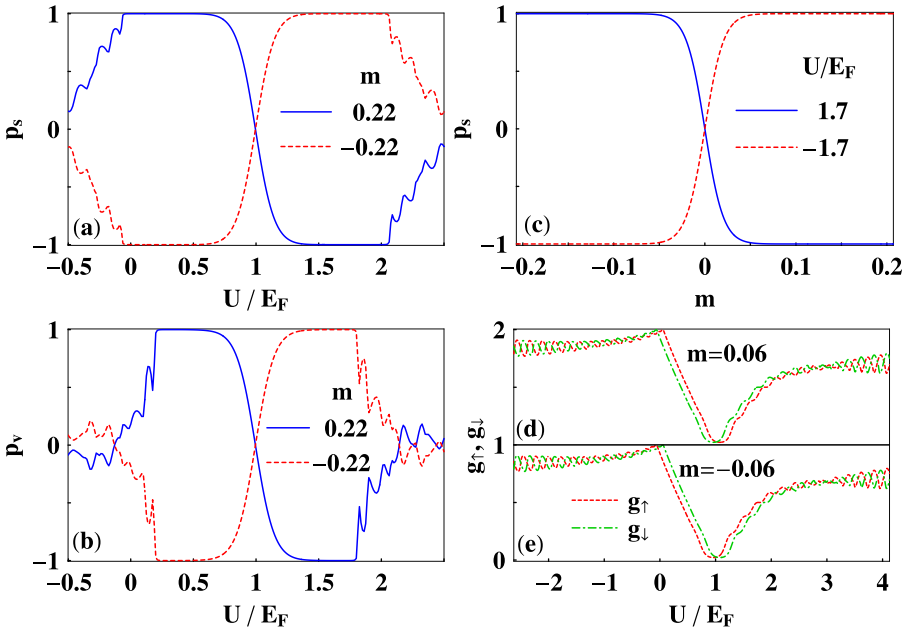

FIG. 10. (a) Spin polarization p_s as a function of U/E_F for $\delta_z = 8$ and $m = \pm 0.22$. Note that p_s is inverted when the direction of the exchange field is reversed. (b) The same as in (a) but for the valley polarization p_v. (c) Spin polarization p_s as a function of m for $U/E_F = \pm 1.7$. (d) Conductances $g_\uparrow$ and $g_\downarrow$ as functions of U/E_F for $m = \pm 0.06$.

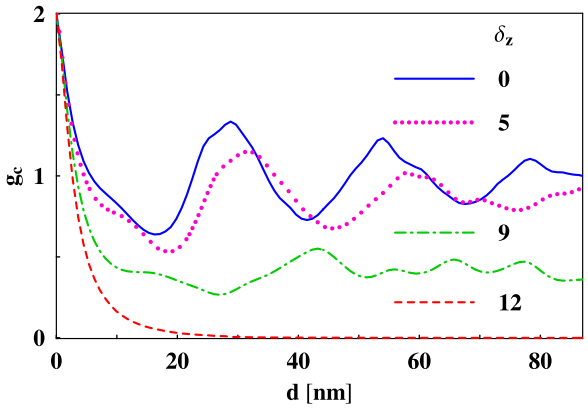

FIG. 11. Charge conductance g_c as a function of the barrier width d for increasing values of δ_z. The critical value is $\delta_z^c = 11.9$ and $m_1 = m_2 = 0.063$.

(see Fig. 6(b)). This is also reflected in the oscillations of g_c which are also slightly irregular.

In Fig. 13(b), we show $g_\uparrow$, $g_\downarrow$, and g_c as functions of V/E_F with the exchange fields in opposite directions, $m_1 = 0.05$ and $m_2 = -0.05$. Interestingly, we find that $g_\uparrow$ becomes identical to $g_\downarrow$, i.e., the exchange fields do not shift $g_\uparrow$ and $g_\downarrow$ relative to each other. It is as if the exchange fields have opposite effects. This is due to the particular combination of M_i and s_z which enters the wave vectors $k_F^{(i)}$. Specifically, the effect of a positive M_i on spin-up electrons is identical to that of a negative M_i on spin-down electrons, i.e., $s_z M_i$ is positive in both cases. This explains the equality $g_\uparrow = g_\downarrow$ and the absence of splitting in g_c. The absence of splittings leads to zero spin polarization through the double junction. At the same time, we note that the amplitudes of the oscillations in $g_\uparrow$ and $g_\downarrow$ are strongly suppressed.

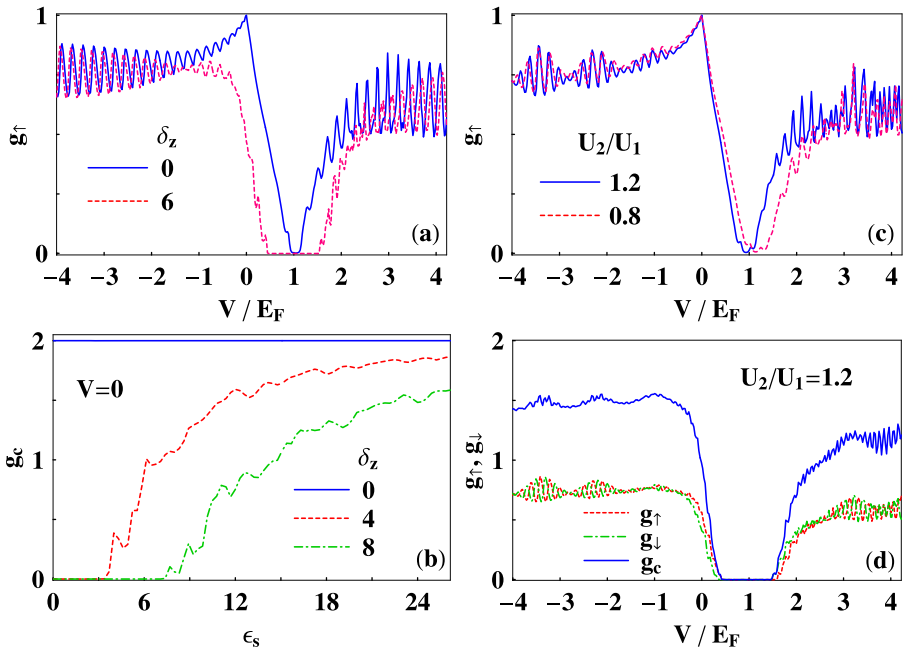

FIG. 12. (a) Spin-up conductance $g_\uparrow$ as a function of V/E_F with $U_1 = U_2 = V$ and $m_1 = m_2 = 0$. (b) Charge conductance g_c as a function of $\epsilon_s = E_F/\lambda_{so}$ for $V = 0$ and increasing values of δ_z. (c) $g_\uparrow$ versus V/E_F for $U_1 = V$, two values of U_2/U_1, and $\delta_z = m = 0$. (d) Conductances $g_\uparrow$, $g_\downarrow$, and g_c versus V/E_F for $\delta_z = 6$ and $m_1 = m_2 = 0.05$.

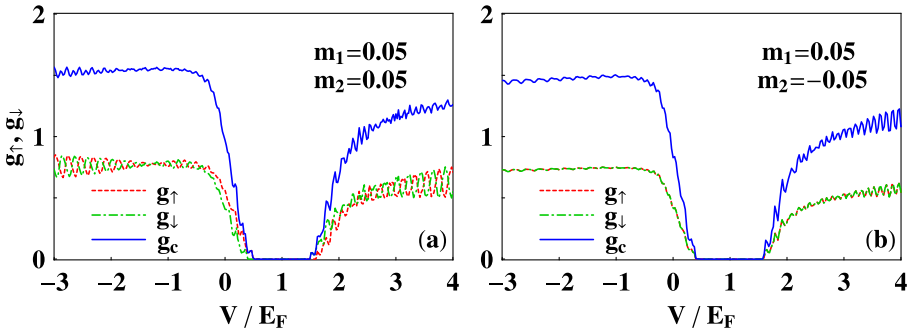

FIG. 13. (a) Spin-resolved conductances $g_\uparrow$ and $g_\downarrow$, and charge conductance g_c as functions of V/E_F for $U_1 = U_2$, $\delta_z^{(1)} = \delta_z^{(2)} = 6$, and $m_1 = m_2 = 0.05$. (b) The same as in (a) but for $m_1 = 0.05$ and $m_2 = -0.05$.

V. SUMMARY

We studied ballistic transport through silicene single or double ferromagnetic junctions and showed that they exhibit novel phenomena that are distinct from their counterparts in graphene. In particular, we showed that the charge conductance g_c can be tuned by an external perpendicular electric field E_z. Above a critical E_z, g_c changes from an oscillatory to a monotonically decreasing function of the junction width d. We also showed that g_c develops a transport gap with increasing E_z. These novel features could be used for the realization of electric-field-controlled switching.

Furthermore, it was shown that the presence of the ferromagnetic insulator induces exchange splittings in the peaks of g_c, and g_c is a periodic function of the barrier potential U and of the exchange field M. The periodicity of g_c in M offers an alternative method for the experimental determination of M for which exchange splittings can be observed. Importantly, fully spin-polarized current can be achieved near the Dirac point for sufficiently large E_z or M. The spin and valley polarizations can be inverted by changing either the gate voltage U, from negative to positive, or by reversing the direction of M. As for the value $M = 2.32$ meV, it is a little lower than that reported for graphene.[21] These findings could be used to realize a high efficiency silicene-based spin and valley filters. We have also verified numerically, using the finite-temperature version of Eq. (11), that our results are not affected for temperatures up to $T \approx 120$ K provided scattering by phonons or impurities is negligible.

For a double ferromagnetic junction, we showed that g_c can also be tuned by E_z. Furthermore, for wells with unequal depths, we found that the conductance exhibits a beating pattern which is attributed to interference effects of Dirac fermions with slightly different energies. The directions of the magnetizations play a significant role. Specifically, when the exchange fields in the two junctions are in opposite directions but have equal magnitudes, the $g_\uparrow$ conductance becomes identical to the $g_\downarrow$ one and there is no exchange splitting in the charge conductance g_c. We expect that our results will be tested by appropriate experiments.

ACKNOWLEDGMENTS

Our work was supported by the Canadian NSERC Grant No. OGP0121756.

APPENDIX A: CONDUCTANCE AT THE DIRAC POINT

The dip in the conductances $g_\uparrow$, $g_\downarrow$ shown in Fig. 2 originates from the dominant contribution of evanescent modes near the DP. As a result, the conductance is suppressed and can be made to vanish by increasing either the barrier width d or the electric field. In the first case $g_{\xi s_z} \to 0$ because d increases while, in the second case, $|k_x'|$ increases [see Eqs. (6) and (9)]. In order to show this, it is convenient to introduce the dimensionless variable

$$\eta = [E_F - U + s_z M]/[E_F^2 - \lambda_{so}^2]^{1/2} \tag{A1}$$

as a measure of the gate voltage U. By setting $u = \sin\theta$ the transmission probability (8) takes the form

$$T_{\xi s_z}(u) = (1-u^2)(\eta_\delta^2 - u^2)/\{(1-u^2)(\eta_\delta^2 - u^2)\cos^2(k_x' d) + (1/4)\sin^2(k_x' d)[p + \eta_\delta^2 p^{-1} - 2u^2]^2\}, \tag{A2}$$

where $\eta_\delta = (\eta^2 - \delta_{\xi s_z}^2)^{1/2}$, $\delta_{\xi s_z} = \Delta_{\xi s_z}/(E_F^2 - \lambda_{so}^2)^{1/2}$ and $p = [\eta(E_F^2 - \lambda_{so}^2)^{1/2} - \Delta_{\xi s_z}]/E_N$. The longitudinal momenta in the barrier region k_x' can be expressed as

$$k_x' = k_F[\eta_\delta^2 - u^2]^{1/2}. \tag{A3}$$

In the following we set $M = 0$ in Eq. (A1) for simplicity. At the DP, i.e., for $\eta = 0$ in Eq. (A2), we get $p + \eta_\delta^2 p^{-1} - 2u^2 \approx -2u^2$ assuming $E_F \gg \lambda_{so}$. Also $k_x' = ik_F\delta_\alpha$ with $\delta_\alpha = (\delta_{\xi s_z}^2 + u^2)^{1/2}$. For $k_F d \gg 1$ and $\delta_{\xi s_z}^2 + u^2 \approx \delta_{\xi s_z}^2$ we obtain

$$T_{\xi s_z}(u) \approx 4e^{-2k_F d\delta_\alpha}. \tag{A4}$$

From Eq. (A3) it can be seen that k_x' can be either real ($\eta_\delta^2 > u^2$) or purely imaginary ($\eta_\delta^2 < u^2$), corresponding to propagating and evanescent modes, respectively. For $|\eta_\delta| < 1$, the conductance can be split into the contributions from propagating and evanescent modes,

$$g_{\xi s_z} = \int_0^1 du T_{\xi s_z}(u) = \int_0^{|\eta_\delta|} du T_{\xi s_z}(u) + \int_{|\eta_\delta|}^1 du T_{\xi s_z}(u) = g_{\xi s_z}^{\text{prop}} + g_{\xi s_z}^{\text{evan}}. \tag{A5}$$

From Eq. (A5) it is seen that the contribution to the conductance from the evanescent modes becomes dominant in the region near $\eta_\delta = 0$. In fact $\eta_\delta = 0$ gives the critical electric

field $\Delta_z^c = \xi s_z \lambda_{so} \pm |E_F - U + s_z M|$ mentioned in Sec. II B. Inserting Eq. (A4) into Eq. (A5) and using $\delta_\alpha \approx |\delta_{\xi s_z}| + u^2/2|\delta_{\xi s_z}|$ we find

$$g_{\xi s_z} \approx (4\pi/q)^{1/2} e^{-2k_F d|\delta_{\xi s_z}|} \mathrm{erf}(\sqrt{q}), \tag{A6}$$

where $q = k_F d/|\delta_{\xi s_z}|$; erf$(x)$ is the error function. Equation (A6) is in very good agreement with the exact numerical calculation presented in Fig. 4(b) as long as $\delta_{\xi s_z} \sim \Delta_{\xi s_z} \neq 0$. It can be seen that, for any spin or valley index, $g_{\xi s_z}$ exhibits a monotonically decaying dependence on δ_z as long as $\delta_z > 1$. It also exhibits a similar dependence on the width d of the barrier for fixed δ_z.

APPENDIX B: CONDUCTANCE FOR STRONG POTENTIALS

For high barriers or deep wells, $|\eta| \gg 1$, using $u^2 \leq 1$ we have $u^2/\eta^2 \to 0$. Also in Eq. (A2) we have

$$p + \eta_\delta^2 p^{-1} - u^2 \simeq 2\eta, \tag{B1}$$

where we assumed that $E_F \gg \lambda_{so}$. Also $k_x' d \simeq k_F d \eta \delta_\lambda$ with $\delta_\lambda = [1 - (\delta_{\xi s_z}^2/\eta^2)]^{1/2}$. Then, with $\delta_\beta^2 = \delta_{\xi s_z}^2/\eta^2$ and $\omega = k_F d \eta \delta_\lambda$, Eq. (A2) takes the form

$$T_{\xi s_z}(u) \simeq \frac{1 - \left(\delta_\beta^2 + u^2 - \delta_\beta^2 u^2\right)}{1 - \left(\delta_\beta^2 + u^2 - \delta_\beta^2 u^2\right)\cos^2\omega}. \tag{B2}$$

Inserting Eq. (B2) in Eq. (A5) we get

$$g_{\xi s_z} \simeq \frac{|\gamma| - (1 - \gamma^2)\mathrm{arctanh}(|\gamma|)}{|\gamma| \cos^2\omega}, \tag{B3}$$

where $\gamma = \delta_\lambda \cos\omega/[1 - \delta_\beta^2 \cos^2\omega]^{1/2}$. We notice that this $g_{\xi s_z}$ is periodic in the variable η with period $\pi/k_F d \delta_\lambda$. Equation (B3) is in very good agreement with the exact numerical calculation for either zero or finite δ_z and M.

[1]G. G. Guzmán-Verri and L. C. Lew Yan Voon, Phys. Rev. B **76**, 075131 (2007); S. Lebègue and O. Eriksson, Phys. Rev. B **79**, 115409 (2009).
[2]P. Vogt, P. De Padova, C. Quaresima, J. Avila, E. Frantzeskakis, M. C. Asensio, A. Resta, B. Ealet, and G. Le Lay, Phys. Rev. Lett. **108**, 155501 (2012); A. Fleurence, R. Friedlein, T. Ozaki, H. Kawai, Y. Wang, and Y. Yamada-Takamura, *ibid.* **108**, 245501 (2012).
[3]D. Chiappe, E. Scalise, E. Cinquanta, C. Grazianetti, B. V. Broek, M. Fanciulli, M. Houssa, and A. Molle, Adv. Mater. **26**, 2096 (2014).
[4]Z. Ni, Q. Liu, K. Tang, J. Zheng, J. Zhou, R. Qin, Z. Gao, D. Yu, and J. Lu, Nano Lett. **12**, 113 (2012); Y. Cai, C.-P. Chuu, C. M. Wei, and M. Y. Chou, Phys. Rev. B **88**, 245408 (2013); M. Neek-Amal, A. Sadeghi, G. R. Berdiyorov, and F. M. Peeters, Appl. Phys. Lett. **103**, 261904 (2013); H. Liu, J. Gao, and J. Zhao, J. Phys. Chem. C **117**, 10353 (2013).
[5]A. H. Castro Neto, F. Guinea, N. M. R. Peres, K. S. Novoselov, and A. K. Geim, Rev. Mod. Phys. **81**, 109 (2009).
[6]C.-C. Liu, W. Feng, and Y. Yao, Phys. Rev. Lett. **107**, 076802 (2011).
[7]N. D. Drummond, V. Zólyomi, and V. I. F'alko, Phys. Rev. B **85**, 075423 (2012).
[8]M. Ezawa, New J. Phys. **14**, 033003 (2012).
[9]A. Dyrdał and J. Barnas, Phys. Status Solidi RRL **6**, 340 (2012).
[10]M. Tahir, A. Manchon, K. Sabeeh, and U. Schwingenschlögl, Appl. Phys. Lett. **102**, 162412 (2013).
[11]C. J. Tabert and E. J. Nicol, Phys. Rev. B **87**, 235426 (2013).
[12]X.-T. An, Y.-Y. Zhang, J.-J. Liu, and S.-S. Li, Appl. Phys. Lett. **102**, 043113 (2013).
[13]M. Ezawa, Phys. Rev. Lett. **109**, 055502 (2012).
[14]L. Stille, C. J. Tabert, and E. J. Nicol, Phys. Rev. B **86**, 195405 (2012).
[15]A. Kara, H. Enriquez, A. P. Seitsonen, L. C. Lew Yan Voon, S. Vizzini, B. Aufray, and H. Oughaddoub, Surf. Sci. **67**, 1 (2012).
[16]C.-C. Liu, H. Jiang, and Y. Yao, Phys. Rev. B **84**, 195430 (2011).
[17]B. Huang, D. J. Monsma, and I. Appelbaum, Phys. Rev. Lett. **99**, 177209 (2007).
[18]Y. Wang, J. Zheng, Z. Ni, R. Fei, Q. Liu, R. Quhe, C. Xu, J. Zhou, Z. Gao, and J. Lu, Nano **7**, 1250037 (2012).
[19]S. Sanvito, Chem. Soc. Rev. **40**, 3336 (2011).
[20]N. Tombros, C. Jozsa, M. Popinciuc, H. T. Jonkman, and B. J. van Wees, Nature **448**, 571 (2007).
[21]H. Haugen, D. Huertas-Hernando, and A. Brataas, Phys. Rev. B **77**, 115406 (2008).
[22]J. Milton Pereira, Jr., P. Vasilopoulos, and F. M. Peeters, Appl. Phys. Lett. **90**, 132122 (2007).
[23]T. Yokoyama, Y. Tanaka, and N. Nagaosa, Phys. Rev. B **81**, 121401(R) (2010).
[24]H. Pan, Z. Li, C.-C. Liu, G. Zhu, Z. Qiao, and Y. Yao, Phys. Rev Lett. **112**, 106802 (2014).
[25]S. Mondal, D. Sen, K. Sengupta, and R. Shankar, Phys. Rev. Lett. **104**, 046403 (2010).
[26]T. Yokoyama, Phys. Rev. B **87**, 241409(R) (2013).
[27]B. Soodchomshom, J. Appl. Phys. **115**, 023706 (2014).
[28]M. Ezawa, Phys. Rev. B **87**, 155415 (2013).
[29]V. Vargiamidis and P. Vasilopoulos, Appl. Phys. Lett. **105**, 223105 (2014).
[30]P. G. Silvestrov and K. B. Efetov, Phys. Rev. Lett. **98**, 016802 (2007).
[31]L. Liu, Y.-X. Li, Y.-T. Zhang, and J.-J. Liu, J. Appl. Phys. **115**, 023704 (2014).